Mechanisms of seizure propagation in a cortical model

**Mark A. Kramer · Andrew J. Szeri · James W. Sleigh ·
Heidi E. Kirsch**

Abstract We consider a mathematical model of meso-
scopic human cortical ictal electrical activity. We compare
the model results with ictal electrocortical data recorded from
three human subjects and show how the two agree. We deter-
mine that, in the model system, seizures result from increased
connectivity between excitatory and inhibitory cell popula-
tions, or from decreased connectivity within either excita-
tory or inhibitory cell populations. We compare the model
results with the disinhibition and 4-AP models of epilepsy
and suggest how the model may guide the development of
new anticonvulsant therapies.

Keywords Epilepsy · Seizure · Electrocortiogram ·
Human · Mesoscopic cortical dynamics

M. A. Kramer · A. J. Szeri
Applied Science and Technology Graduate Group, University
of California, Berkeley, CA, 94720-1740, USA
Present address MAK:
Center for BioDynamics, 111 Cummington Street, Boston
University, Boston, MA, 02215, USA

A. J. Szeri (✉)
Department of Mechanical Engineering, University of California,
Berkeley, CA, 94720-1740, USA
e-mail: Andrew.szeri@barkley.edu

J. W. Sleigh
Waikato Clinical School, Waikato Hospital,
Hamilton, New Zealand

H. E. Kirsch
Department of Neurology, University of California,
San Francisco, CA, 94143-0138, USA

Introduction

Epilepsy—recurrent unprovoked seizures—affects 2.5 mil-
lion Americans (http://www.epilepsyfoundation.org/, 2005).
Of these, approximately 20% experience medically refrac-
tory epilepsy and may undergo resective surgery to remove
the epileptogenic zone—the brain region responsible for
seizure generation. Before performing this surgery, physi-
cians must first locate the epileptogenic zone. To do so,
they may perform noninvasive (e.g., scalp electroencephalo-
gram (EEG)) and invasive (e.g., electrocortiogram (ECoG))
recordings of cortical electrical activity. Invasive ECoG
recording may be done intraoperatively to capture interictal
epileptiform activity or chronically—using implanted sub-
dural electrodes—to capture ictal activity. The latter clini-
cal scenario offers researchers the rare opportunity to study
pathological, organized cortical electrical activity.

To further understand human cortical electrical activity
recorded during a seizure, researchers have developed nu-
merous models. Many models derive from animal studies, in
which invasive single-unit recordings are made while chem-
ical manipulations are performed. Elaborate mathematical
models exist to describe the behavior of single neurons and
networks of individual neurons during a seizure (Traub et al.,
2005). Here we are interested in the ECoG data recorded
from a seizing human subject. To model this data—recorded
at a single electrode, say—we would like to simulate the
behavior of approximately 10^5 individual neurons (Nunez
and Cutillo, 1995). Unfortunately, using physiologically ac-
curate mathematical models, we find such simulations com-
putationally infeasible.

Therefore, we implement a mathematical model of *meso-
scopic* cortical electrical activity. Mesoscopic models—
unlike models of single neuron behavior such as
the Hodgkin–Huxley equations—approximate the average

activity or mean-field generated by cell populations. To develop these models, researchers determine expressions describing the spatially averaged properties of neighboring neurons (Wilson and Cowan, 1972; Freeman, 1964). The resulting variables and parameters describe, for example, the spatial average of the soma membrane potential of a cell population or the average subcortical input received by a volume of cortex. In these models, the smallest unit of activity is the cell population, not the individual neuron.

There are (at least) two reasons for implementing a mesoscopic model of human ECoG data. First, the electrocortiograph records the summed electrical activity from millions of individual neurons. Therefore the mesoscopic model and ECoG recordings produce simulated and observed results, respectively, at a similar spatial scale. Second, some researchers believe that cortical columns—not individual neurons—form the effective units of cortical operation (Singer, 1993; Mountcastle, 1997). A cortical column consists of all tissue (e.g., neurons, glia cells, axons) within a cylindrical volume of approximate area 1 mm^2 at the cortical surface and extending radially inward through all layers of cortex. Using a mesoscopic model, we describe the electrical activity produced by cortical columns, not individual neurons.

In what follows, we describe one such mathematical model of mesoscopic cortical electrical activity. We compare the model results with ictal ECoG data recorded from three human subjects and show that the observational and simulated results agree in two important ways during seizure: the frequency of maximum power, and the speed of voltage propagation over the cortex. We also show that both quantities (and the variability) change during the course of a seizure and that we may account for these changes in the model. Finally, we discuss changes in the model parameters that result in seizure-like oscillations in the dynamics. We will show that seizures result in the model system from increased connectivity between the excitatory and inhibitory cell populations, or decreased connectivity within the excitatory population or within the inhibitory population. We compare the model results with the disinhibition hypothesis, and with induction and suppression of seizures by 4-aminopyridine (4-AP) and benzodiazepines (BZ), respectively. For the latter pharmacological manipulations, we use the model to suggest the mechanisms of action.

Methods

Mathematical model

To model human cortical electrical activity we implement a system of eight, nonlinear, stochastic partial differential equations (SPDEs) and twenty parameters presented in

Kramer et al. (2005) by recasting in dimensionless form the equations stated in Steyn-Ross et al. (2003). We restate the system here:

$$\frac{\partial \tilde{h}_e}{\partial \tilde{t}} = 1 - \tilde{h}_e + \Gamma_e \left(h_e^0 - \tilde{h}_e \right) \tilde{I}_{ee} + \Gamma_i \left(h_i^0 - \tilde{h}_e \right) \tilde{I}_{ie} \quad \text{(1a)}$$

$$\frac{\partial \tilde{h}_i}{\partial \tilde{t}} = 1 - \tilde{h}_i + \Gamma_e \left(h_e^0 - \tilde{h}_i \right) \tilde{I}_{ei} + \Gamma_i \left(h_i^0 - \tilde{h}_i \right) \tilde{I}_{ii} \quad \text{(1b)}$$

$$\left(\frac{1}{T_e} \frac{\partial}{\partial \tilde{t}} + 1 \right)^2 \tilde{I}_{ee} = N_e^\beta \tilde{S}_e[\tilde{h}_e] + \tilde{\phi}_e + P_{ee} + \tilde{\Gamma}_1 \quad \text{(1c)}$$

$$\left(\frac{1}{T_e} \frac{\partial}{\partial \tilde{t}} + 1 \right)^2 \tilde{I}_{ei} = N_e^\beta \tilde{S}_e[\tilde{h}_e] + \tilde{\phi}_i + P_{ei} + \tilde{\Gamma}_2 \quad \text{(1d)}$$

$$\left(\frac{1}{T_i} \frac{\partial}{\partial \tilde{t}} + 1 \right)^2 \tilde{I}_{ie} = N_i^\beta \tilde{S}_i[\tilde{h}_i] + P_{ie} + \tilde{\Gamma}_3 \quad \text{(1e)}$$

$$\left(\frac{1}{T_i} \frac{\partial}{\partial \tilde{t}} + 1 \right)^2 \tilde{I}_{ii} = N_i^\beta \tilde{S}_i[\tilde{h}_i] + P_{ii} + \tilde{\Gamma}_4 \quad \text{(1f)}$$

$$\left(\frac{1}{\lambda_e} \frac{\partial}{\partial \tilde{t}} + 1 \right)^2 \tilde{\phi}_e = \frac{1}{\lambda_e^2} \frac{\partial^2 \tilde{\phi}_e}{\partial \tilde{x}^2} + \left(\frac{1}{\lambda_e} \frac{\partial}{\partial \tilde{t}} + 1 \right) N_e^\alpha \tilde{S}_e[\tilde{h}_e] \quad \text{(1g)}$$

$$\left(\frac{1}{\lambda_i} \frac{\partial}{\partial \tilde{t}} + 1 \right)^2 \tilde{\phi}_i = \frac{1}{\lambda_i^2} \frac{\partial^2 \tilde{\phi}_i}{\partial \tilde{x}^2} + \left(\frac{1}{\lambda_i} \frac{\partial}{\partial \tilde{t}} + 1 \right) N_i^\alpha \tilde{S}_e[\tilde{h}_e]. \quad \text{(1h)}$$

The eight dynamical variables in this system ($\tilde{h}_e$, $\tilde{h}_i$, $\tilde{I}_{ee}$, $\tilde{I}_{ei}$, $\tilde{I}_{ie}$, $\tilde{I}_{ii}$, $\tilde{\phi}_e$, and $\tilde{\phi}_i$) are functions of dimensionless space and time, $\tilde{x}$ and $\tilde{t}$, respectively. We define the dimensionless variables and parameters in Tables 1 and 2, respectively, and note that in *Results* we relabel some parameters to allow more specific manipulations. The interested reader may find an implementation of this model written in IDL (Interactive Data Language) at *http://makramer.info*.

Equation (1a) relates the evolution of the (dimensionless) voltage of the excitatory population to: the voltage itself ($\tilde{h}_e$), the dimensionless excitatory input current ($\tilde{I}_{ee}$), and the dimensionless inhibitory input current ($\tilde{I}_{ie}$). Equations (1c) and (1e) define the dynamical rules of these input currents. The excitatory input current ($\tilde{I}_{ee}$) evolves according to local input ($N_e^\beta \tilde{S}_e[\tilde{h}_e]$), distant excitatory cortical input ($\tilde{\phi}_e$), subcortical input (P_{ee}), and stochastic input ($\tilde{\Gamma}_1$). The term $\tilde{S}_e[\tilde{h}_e]$ is a dimensionless sigmoid transfer function:

$$\tilde{S}_e[\tilde{h}_e] = \frac{1}{1 + \exp[-\tilde{g}_e(\tilde{h}_e - \tilde{\theta}_e)]}, \quad \text{(2)}$$

that acts to convert the local voltage of the excitatory population into a mean firing rate of the excitatory population (i.e., a "wave-to-pulse" conversion (Liley et al., 2002)). The distant cortical input—which is always excitatory—evolves

Table 1 Dynamical variable definitions for the dimensionless SPDEs model. The dimensionless variables (left column) are defined in terms of the dimensional symbols (middle column) found in Table 1 of Steyn-Ross et al. (2003). The variables are described in the right column. Sub-scripts e and i refer to excitatory and inhibitory. We make the notational simplifications in agreement with the values used in Steyn-Ross et al. (2003): $\tau_e = \tau_i = \tau$, $S_e^{max} = S_i^{max} = S^{max}$, and $h_e^{rest} = h_i^{rest} = h^{rest}$

Symbol	Definition	Description
$\tilde{h}_{e,i}$	$h_{e,i}/h^{rest}$	Population mean soma dimensionless electric potential
$\tilde{I}_{ee,ie}$	$I_{ee,ie}\gamma_e/(G_e \exp(1)S^{max})$	Total $e \to e$, $i \to e$ input to excitatory populations
$\tilde{I}_{ei,ii}$	$I_{ei,ii}\gamma_i/(G_i \exp(1)S^{max})$	Total $e \to i$, $i \to i$ input to inhibitory populations
$\tilde{\phi}_{e,i}$	$\phi_{e,i}/S^{max}$	Long range (corticocortical) input to e, i populations
$\tilde{t}$	t/τ	Dimensionless time
$\tilde{x}$	$x/(\tau\tilde{v})$	Dimensionless space

Table 2 Parameter values for the dimensionless SPDEs neural macro-column model. The dimensionless symbols (first column) are defined in terms of the dimensional variables (second column) found in Table 1 of Steyn-Ross et al. (2003). The variables are described in the third column and typical values are shown in the fourth column. We make the notational simplifications in agreement with the values used in Steyn-Ross et al. (2003): $\tau_e = \tau_i = \tau$, $S_e^{max} = S_i^{max} = S^{max}$, and $h_e^{rest} = h_i^{rest} = h^{rest}$

Symbol	Definition	Description	Typical value
e, i		(As subscript) excitatory, inhibitory cell populations	
$\Gamma_{e,i}$	$\dfrac{G_{e,i}\exp(1)S^{max}}{\gamma_{e,i}\lvert h_{e,i}^{rev} - h^{rest}\rvert}$	Influence of input on the mean soma membrane values	$1.42 \times 10^{-3}, 0.0774$
$h_{e,i}^0$	$h_{e,i}^{rev}/h^{rest}$	Dimensionless cell reversal potential	$-0.643, 1.29$
$T_{e,i}$	$\tau\gamma_{e,i}$	Dimensionless neurotransmitter rate constant	$12.0, 2.6$
$\lambda_{e,i}$	$\tau\tilde{v}\Lambda_{ee,ei}$	Dimensionless characteristic corticocortical inverse-length scale	$11.2, 18.2$
$P_{ee,ie}$	$p_{ee,ie}/S^{max}$	Subcortical input to e population	$11.0, 16.0$
$P_{ei,ii}$	$p_{ei,ii}/S^{max}$	Subcortical input to i population	$16.0, 11.0$
$N_{e,i}^{\alpha}$	–	Total number of synaptic connections from distant e populations	$4000, 2000$
$N_{e,i}^{\beta}$	–	Total number of local e and i synaptic connections	$3034, 536$
$\tilde{g}_{e,i}$	$g_{e,i}h^{rest}$	Dimensionless sigmoid slope at inflection point	$-19.6, -9.8$
$\tilde{\theta}_{e,i}$	$\theta_{e,i}/h^{rest}$	Dimensionless inflection point for sigmoid function	$0.857, 0.857$

according to a reaction diffusion type equation defined in (1g). This expression results as an approximation to an integral of synaptic input over the cortical surface. To represent unknown subcortical inputs, the last term $\tilde{\Gamma}_1$ in (1c) is included. We define this dimensionless stochastic input term:

$$\tilde{\Gamma}_1 = \alpha_{ee}\sqrt{P_{ee}}\,\xi_1[\tilde{x}, \tilde{t}]. \tag{3}$$

Here ξ_1 is a Gaussian distributed white noise source with zero mean. In numerical simulations, we approximate the ξ_1 as,

$$\xi_1[\tilde{x}, \tilde{t}] = \frac{R(m, n)}{\sqrt{\Delta\tilde{x}\Delta\tilde{t}}}, \tag{4}$$

where $\tilde{x} = m\Delta\tilde{x}$ and $\tilde{t} = n\Delta\tilde{t}$, $(m, n$ integers), specify space and time coordinates on a lattice with (dimensionless) grid spacing, $\Delta\tilde{x}$ and $\Delta\tilde{t}$, respectively. Similar equations hold for the dynamics of the inhibitory population (1b), local inputs to the inhibitory population (1d) and (1f), and distant excitatory inputs to the inhibitory population (1h).

The main observable in the model is the (dimensional) variable h_e—the spatially averaged soma membrane poten-

tial of excitatory cortical cells. In terms of the *dimensionless* variable in (1): $h_e = \tilde{h}_e \times (-70$ mV$)$. To relate h_e to observational data, we first note that the electrocortiograph records a spatial average of the local field potentials generated within the cortex. We then note that these local field potentials—generated by cell populations—are proportional to the negative deviation of the spatially averaged soma membrane potential of excitatory cortical neurons (i.e., h_e) from rest (Liley et al., 2002). Therefore, the observed ECoG data are proportional to the model variable h_e.

In Kramer et al. (2005) we compared the variable h_e to ictal ECoG data recorded from a human subject. We showed that—for certain parameter values—the model results and ECoG data agreed in two important ways during seizure: f_0—the frequency of maximum power, and v—the speed of voltage propagation across the cortex. We briefly describe the model results. To induce seizure-like activity in the model dynamics, we changed two parameters related to the excitation of the model. We increased the parameter P_{ee}—the strength of the excitatory subcortical input to excitatory cells in the cortex—by a large amount (e.g., 2000%), and decreased the parameter Γ_e—the influence of excitatory input on the mean soma membrane potentials of excitatory and

inhibitory cells—by a small amount (e.g., 30%). We then computed numerical solutions to the SPDEs in (1) for one-spatial dimension and found that traveling waves of activity developed in h_e. To understand the nature of the transitions resulting in this activity, we considered a simplified formulation of (1) without stochastic input (the $\tilde{\Gamma}_k$ terms) and without spatial dependence. In this ordinary differential equations (ODEs) version of the model, we found that abrupt transitions from stable fixed points in h_e to large amplitude, stable oscillations in h_e occurred near subcritical Hopf bifurcations. (The unstable limit cycles born in the Hopf bifurcations stabilized in saddle node bifurcations of limit cycles (Kramer et al., 2005, 2006)). We interpreted these Hopf bifurcations in the model dynamics as the correlates of seizures on the real human cortex. From numerical simulations of the ODEs and the complete SPDEs we deduced approximations for the frequency of oscillation and the speed of (one-dimensional) propagation of h_e during *"seizure"*. We found $f_0 \approx 10$ Hz and $v \approx 2$ m/s over a broad range of (Γ_e, P_{ee}) combinations.

Analysis methods

We compare the model results for f_0 and v with results calculated from ECoG data recorded from three seizing human subjects. To do so, we apply two measures—the windowed power spectra (WPS) and windowed cross-correlation (WCC). To calculate the WPS, we first bandpass filter the ECoG data recorded at each electrode between 1.0 Hz and 55.0 Hz. We then partition the ECoG data into overlapping temporal windows of duration 1.0 s and overlap 0.5 s, multiply the data in each window by the Hanning function, and calculate the power spectrum within each window. We store the resulting power spectra in a two-dimensional array, with frequency along one axis and the center time of each window along the other. Analyzing this WPS array, we observe changes in the power spectra recorded at each electrode over time. To compute f_0, we first determine the frequency of maximum power within each window. We then average these frequencies of maximum power over two subsets of windows (or equivalently two intervals of time). The first interval—I1—begins at seizure onset and ends 10 s later. The second—I2—begins 10 s after seizure onset and ends at seizure termination. We will indicate the usefulness of the two intervals in *Results*. Within each interval, we label the average frequency of maximum power f_0. We repeat this calculation for each seizure recorded from a subject and average the results for f_0 in I1 and f_0 in I2 over the seizures.

To compute the WCC, we first filter and partition the data as we already discussed for the WPS calculation. We then compute the cross-correlation between the data recorded at two electrodes within each window. We store the resulting cross-correlations in a two-dimensional array with the time lag along one axis and the center time of each window along the other. We analyze this WCC result to compute the quantity of interest: v. To do so, we first determine the time lag of maximal cross-correlation within each window of the WCC. Next, we average the resulting time lags of maximum correlation over the two intervals I1 and I2. Then we divide the electrode separation (approximately 10 mm or 14.4 mm) by the average time lag to determine v in I1 and I2. We perform this analysis on each seizure recorded from a subject and average the resulting values for v in I1 and for v in I2 over the seizures.

Subjects

In Kramer et al. (2005) we analyzed six seizures recorded from a seizing human subject. We computed two quantities, f_0 (over the entire duration of the seizure) and v, and we found that the observed results—deduced from the WPS and WCC—agreed with the simulation results. Specifically, we found that the frequencies of maximum power f_0 agreed within a factor of 2, and the speeds of voltage propagation v within a factor of 5.

We used the results in Kramer et al. (2005) to suggest that the SPDEs—with appropriate parameter values—can approximate the electrical activity of the seizing human cortex. To explore further the validity of the SPDEs model, we perform here a similar analysis of ictal ECoG data recorded from three human subjects. Each subject suffered from intractable epilepsy and underwent electrode implantation as part of his or her care at the University of California, San Francisco (UCSF) Epilepsy Center. For each subject, a surgeon implanted an 8×8 electrode grid (10 mm spacing in the vertical and horizontal directions) and one or two 6-electrode strips in the subdural space, overlying the cortical surface (also 10 mm spacing). Depth electrodes were also employed, but we do not consider data from the depth electrodes here. All strip and grid electrodes were 4 mm diameter platinum-iridium discs embedded in a 1.5 mm thick silastic sheet with 2.3 mm diameter exposed surfaces and 10 mm spacing between the discs. To observe multiple seizures, physicians recorded ECoG data continuously at 400 Hz for several days from each subject.

In *Results* we present our analysis of the ictal ECoG data recorded from the three subjects. We begin our analysis with Subject A: a 28-year-old man. For this subject physicians implanted an 8×8 electrode grid over the left frontotemporal region and two, 6-electrode subdural strips curled under the left anterior and left posterior temporal lobes. ECoG data, recorded continuously for 15 days, captured two subclinical seizures (i.e., seizures observed in the ECoG but

with no clinical manifestations, such as convulsions). Both seizures arose from the proximal ends of the subtemporal strips.

Next we consider Subject B: a 37 year old woman with an 8×8 electrode grid over her left frontotemporal region, a 6-contact electrode strip over her left suborbital frontal lobe, and two, 6-contact left hippocampal depth electrodes. Physicians recorded ECoG data continuously from this subject for five days and detected nine seizures. Each seizure began near the distal end of both depth electrodes in the hippocampus and, approximately 15 s later, were seen on the electrode grid on the cortical surface.

We conclude with Subject C: a 31 year old woman with an 8×8 electrode grid over her left frontotemporal region, and two, 6-electrode subdural strips curled under her left anterior and left posterior temporal lobe. Physicians recorded ECoG data from this electrode configuration for fourteen days. Three seizures were initially captured. Midway through this recording period, the surgeon inserted an additional 6-contact depth electrode into the left hippocampus. After this, three more seizures were recorded. Each seizure began in the distal end of the posterior left subtemporal electrode strip, and then spread to the distal end of the anterior subtemporal strip (as well as to the hippocampal depth electrode for the last three seizures). After a minute delay, seizure activity appeared on the electrode grid at the frontal portions of the superior and middle temporal gyri.

For each subject we only consider seizure activity manifest on the cortical surface (where the model applies) and from a subset of electrodes identified clinically as the location of cortical seizure onset. We compute f_0 and v for each subject and compare these results with those determined from the mathematical model. In all cases, UCSF and University of California, Berkeley human subject guidelines were observed and patient consent was obtained.

Results

In this section we compare the observational results from three seizing human subjects with results from a mathematical model. Specifically, we compare two quantities: f_0—the frequency of maximum power, and v—the speed of voltage propagation over the cortex during seizure. We have found that $f_0 \approx 10$ Hz and $v \approx 2$ m/s for the mathematical model with a choice of pathological parameter values (as we discussed in *Methods: Mathematical Model*). Here we compute similar quantities—and the variation of each—from the ECoG data and show a qualitative agreement between the observational and model results. We begin with:

Subject A

To compare the observational and model results we follow the procedure in Kramer et al. (2005) and outlined in *Methods* to determine f_0 and v. For Subject A, we analyze ECoG data recorded from one region of seizure initiation identified by the physicians; namely, we consider the three most proximal electrodes on the subdural strip that traverses the inferior aspect of the temporal lobe with the most distal end approximating the parahippocampal gyrus. For convenience, we label these neighboring electrodes a, b, and c, with c the most proximal of the three. We illustrate these WPS results for the second subclinical seizure in Fig. 1. Subfigures (a), (b), and (c) correspond to electrode labels a, b, and c, respectively. Here we plot power in logarithmic greyscale with powers greater than 50 μV^2 in black and less than 0.3 μV^2 in white. We show time in seconds along the horizontal axis and frequency in Hertz along the vertical axis. This subclinical seizure begins at $t = 15$ s; we denote this time with a vertical dashed line in each subfigure. The subclinical seizure continues until $t = 49$ s; we denote the end of the subclinical seizure with a second vertical dashed line in each subfigure. We find that of the three electrodes the middle electrode—shown in Fig. 1(b)—displays the most power (i.e., the darkest regions) during the subclinical seizure. We also note the abrupt decreases in power below 55 Hz both preceding and following the subclinical seizure.

A careful inspection of Figs. 1(a)–(c) suggests that the frequency of maximum power typically decreases slightly through the course of the seizure. To illustrate this, we compute the frequency of maximum power within each time window of the WPS and plot the results for electrodes a, b, and c in Figs. 1(d), (e), and (f), respectively. We indicate the duration of the ictal event with two, vertical dashed lines and divide the subclinical seizure into intervals—I1 and I2—with a vertical dotted line. We note that, for this subclinical seizure, the frequency of maximum power tends to decrease during the ictal event. We quantify this observation in Table 3 where we list the results for f_0 in I1 and I2. We find that the mean values for f_0 lie between 8.2 Hz and 10.0 Hz with a maximum uncertainty in the mean of 0.8 Hz in I1, and between 4.1 Hz and 7.5 Hz with a maximum uncertainty in the mean of 0.4 Hz in I2. We note that the values of f_0 in I1 tend to exceed those in I2 and that the variability in f_0 tends to be larger in I1 than in I2. We will show below that the decreased mean and variability of f_0 during the course of the seizure may be induced in the model by changes in parameters P_{ee} and Γ_e.

The second quantity we determine is the speed of wave propagation v between the middle electrode b and its two neighboring electrodes a and c. To do so we follow the procedure outlined in *Methods* and compute the WCC between
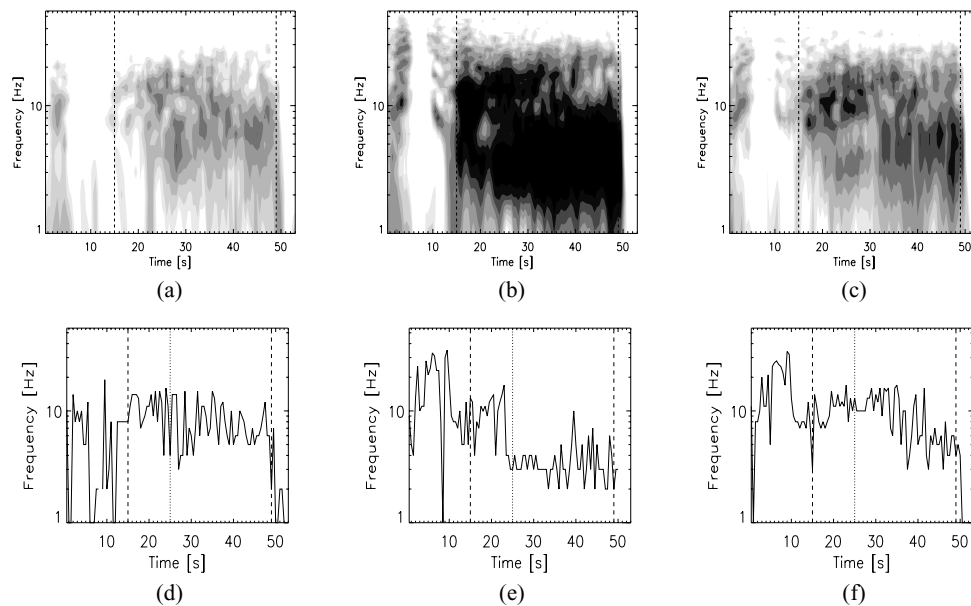
Fig. 1 (a)–(c): The windowed power spectra (WPS) for three ECoG time series recorded during the second subclinical seizure of Subject A. Subfigures (a), (b), and (c) correspond to neighboring electrodes along a subdural strip with (c) the most proximal. The WPS are plotted in logarithmic greyscale with black and white denoting regions of high power (greater than 50 μV^2) and low power (less than 0.3 μV^2), respectively. For the purpose of visual presentation, we smooth the WPS results with a boxcar average of size 1.5 s in time and 3 Hz in frequency.

(d)–(f): The frequency of maximum power plotted as a function of time during the second subclinical seizure. Subfigures (d), (e), and (f) correspond to neighboring electrodes along a subdural strip with (f) the most proximal. In all subfigures, the vertical dashed lines at $t = 15$ s and $t = 49$ s denote the approximate beginning and end of the seizure. We indicate the division between I1 and I2 with a dotted vertical line in the last three subfigures

electrodes b and a, and b and c. We note that here we determine only the one-dimensional component of v along the direction of the subdural electrode grid. We show the results for the second subclinical seizure in Fig. 2 where we plot the WCC between b and a, and b and c in Figs. 2(a) and (b), respectively. In each figure we plot the correlation as a function of time (in s) and time lag (in ms), and indicate the seizure onset with a vertical dashed line, and the location of zero lag

with a horizontal solid line. We show the correlation in linear greyscale, with black denoting regions of correlation greater than 0.8 and white denoting regions of anti-correlation less than -0.8. We found in Kramer et al. (2005) that two intervals (I1 and I2) of wavelike character occurred in the ECoG data recorded from that subject. The same appears to be true here with a different subject. From Fig. 2(a) one notes that the magnitude of the WCC between b and a is not large with
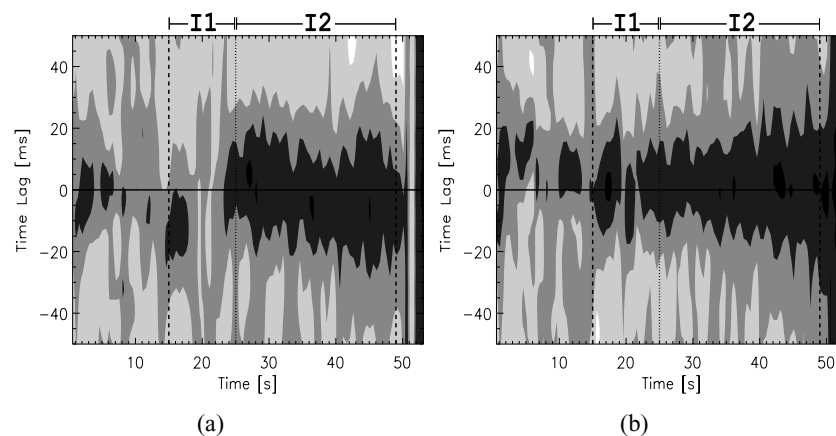
Fig. 2 The windowed cross correlation (WCC) between the ECoG time series recorded from the second subclinical seizure of Subject A. We show in subfigures (a) and (b) the WCC between electrodes b and a, and b and c, respectively. The WCC are plotted in linear greyscale with regions of strong correlation (greater than 0.8) and anti-correlation

(less than -0.8) denoted by black and white, respectively. We denote the seizure onset and termination with vertical dashed lines at the left and right of the figure, respectively. We indicate the boundary between the intervals I1 and I2 with a vertical dotted line. The solid horizontal line denotes the location of zero lag

Table 3 Results for Subject A. The average frequency of maximum power f_0 and average propagation velocity v in I1 and I2 for the ECoG time series data recorded during two subclinical seizures. We label the neighboring electrodes a, b, c, with c most proximal. We compute v from the middle electrode b. To compute the uncertainty in the average, we assume the uncertainties in f_0 and the magnitude of v for each seizure are independent and random and propagate the uncertainties in the standard way. For comparison, we list the approximate values for f_0 and v determined from the mathematical model in the last row (Kramer et al., 2005)

Electrode	f_0 (Hz)		v (m/s)	
	I1	I2	I1	I2
a	9.1 ± 0.6	7.0 ± 0.3	-0.6 ± 0.2	-1.7 ± 0.7
b	8.2 ± 0.8	4.1 ± 0.2	$-$	$-$
c	10.0 ± 0.5	7.5 ± 0.4	7 ± 12	3.4 ± 0.6
Model	~ 10		~ 2 (magnitude)	

any time lag in I1 (i.e., for 15 s $< t <$ 25 s). Only in I2 (i.e., for 25 s $< t <$ 49 s, between the vertical dotted line and the right vertical dashed line in Fig. 2(a)), is the correlation between b and a significant. For electrodes b and c—whose WCC we show in Fig. 2(b)—we find correlations of large magnitude in both I1 and I2.

We list the results for v in the fourth and fifth columns of Table 3, respectively. We note that in I1 the magnitudes of the observational (0.6 m/s and 7 m/s with maximum uncertainty in the mean of 12 m/s) and model (v near 2 m/s) results agree within a factor of four, although we note the large uncertainty in the mean for v between electrodes b and c. We find that in I2 the magnitudes of the observational (1.7 m/s and 3.4 m/s with maximum uncertainty in the mean of 0.7 m/s) and model (v near 2 m/s) results agree within a factor of two. For both intervals, we find that v from b to a is negative, while v from b to c is positive (although we again note the large uncertainty in I1 between electrodes b and c). Thus during seizure a component of the wave appears to propagate in

the proximal direction, from electrodes a to b to c. We note that for Subject A we only collect and analyze data from two subclinical seizures. A larger sample would be preferable for better validation of the model.

Subject B

For Subject B we consider only the electrical activity recorded at the electrode grid because the model applies only to seizure propagation on the cortical surface. Specifically, we investigate a 3×3 subgrid of electrodes identified clinically as a location of cortical seizure onset (the lateral aspect of the middle to posterior left temporal lobe, abutting the temporo-occipital junction.) An analysis of a more inclusive electrode subgrid—or the entire 8×8 electrode grid—may be performed. To consider the usefulness of such an expanded analysis, we compute the maximum value of the cross-correlations between the center electrode of the 3×3 subgrid and all 64 electrodes of the entire 8×8 grid. We sort these values according to increasing electrode separation and plot the results for intervals I1 and I2 in Figs. 3(a) and (b), respectively. We fit each distribution with an exponential of the form: $A \exp[-Bx] + C$, and determine the decay constants B to be 0.37 ± 0.02 cm^{-1} in I1 and 0.25 ± 0.02 cm^{-1} in I2. We note that the distance between two grid electrodes may underestimate the separation between two cortical areas (because of an intervening sulcus, say). Therefore the values for B represent, at best, an upper bound for the decay constants. We also note that in the mathematical model the characteristic length scale of long-range (i.e., cortico-cortical) connections follows an exponential decay with approximate characteristic length scale of 0.4 cm^{-1} (see Fig. 5 of Liley et al. (2002)). We show in Fig. 3 that, even for grid separations greater than 6 cm, the maximum values of these cross-correlations remain greater than 0.2. Thus—for

(a)

(b)
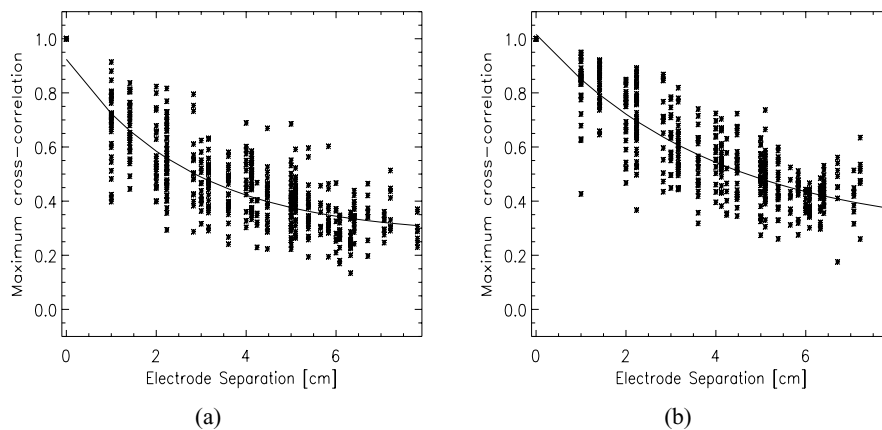
Fig. 3 The maximum value of the cross-correlation as a function of electrode separation (in cm) for Subject B. We compute the cross-correlation between the center electrode of the 3×3 grid and all other grid electrodes during intervals I1 and I2 for each of the subject's eight seizures, and plot the value of maximum cross-correlation for each electrode pair as an asterisk. We plot the exponential fit to each distribution as a solid line. (a) Maximum cross-correlation values in $I1$, (b) maximum cross-correlation values in I2

(a)

(b)
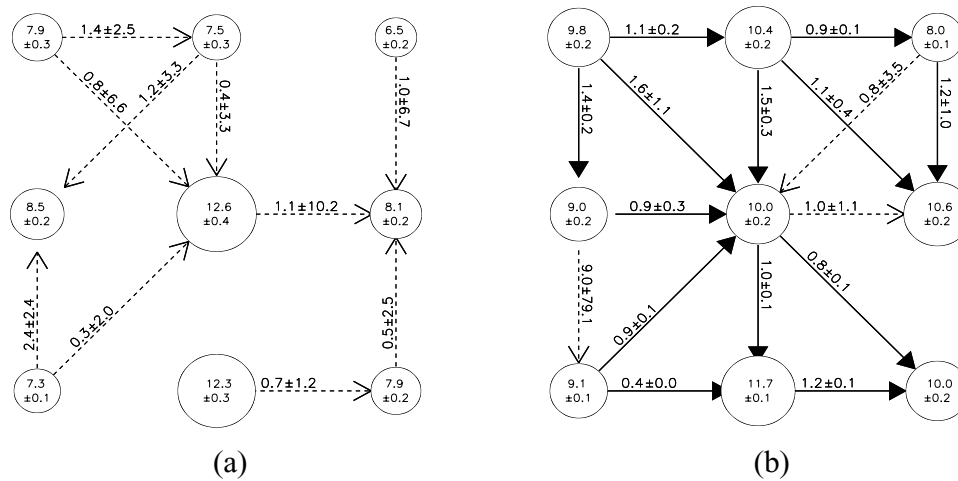
Fig. 4 Results for f_0 and v from Subject B recorded from the 3×3 electrode subgrid on the lateral aspect of the middle to posterior left temporal lobe, abutting the temporo-occipital junction. The radius of each circle corresponds to the mean value of f_0 at the electrode. We write the mean and uncertainty in f_0 (in Hz) within each circle. The arrows indicate the value and uncertainty of v between neighboring electrodes. If the uncertainty in v is less than ten times the magnitude

of v, then we draw an arrow connecting the two electrodes. We indicate the direction of v with the arrow and write the mean value of v and its standard deviation along the line segment. If the mean value of v exceeds one standard deviation from zero, then we draw the line segment solid and the arrowhead filled. Otherwise, we draw the line segment dashed and the arrowhead unfilled. (a) f_0 and v in I1. (b) f_0 and v in I2

Subject B during seizure—the correlation between the initial location of cortical seizure onset and a wide cortical area tends to decay exponentially with distance and asymptotes to a nonzero value. An analysis of an extended subgrid may therefore reveal more characteristics of the frequency and velocity of traveling waves on the seizing cortex. Here, for simplicity, we compare only data recorded from the 3×3 subgrid of clinical interest with the model results.

To determine f_0 we follow the procedure described for Subject A. For each of the nine electrodes in the 3×3 subgrid, we compute the WPS and determine the average frequency of maximum power during the intervals I1 and I2. We repeat this analysis for eight of the subject's seizures (we were unable to extract data for the ninth seizure) and average the results over the seizures to determine f_0 at each electrode. We show the results for the 3×3 subgrid in Fig. 4 where we plot at each grid position a circle whose radius corresponds to the mean value of f_0 at the electrode. We also write the value of f_0 (in Hz) and the uncertainty in the

mean within each circle. We find values for f_0 in I1 between 6.5 Hz and 12.6 Hz, and a maximum uncertainty in the mean of 0.4 Hz, and for f_0 in I2 between 8.0 Hz to 11.7 Hz with a maximum uncertainty in the mean of 0.2 Hz, in agreement with the model results (f_0 near 10 Hz) within a factor of two. We note that, for this subject, the mean values of f_0 are larger in I1 than in I2 for two electrodes (e.g., the center electrode) and smaller for the others (e.g., the left and right columns). We also find that the variability of f_0 appears to be larger in I1 than in I2. To show this, we plot in Fig. 5(a) a histogram of the percentage uncertainty in f_0 for intervals I1 (solid line) and I2 (dashed line). During I1 the percentage uncertainty tends to be larger than during I2. We will compare these results for f_0 with the mathematical model below.

Now we determine v. For Subject A, we computed the component of v in one spatial dimension—along the direction of the subdural electrode strip. In this section, we determine the components of v along the two spatial dimensions of the electrode grid for Subject B. To do so, we compute

Fig. 5 Histogram of the percentage uncertainty in f_0 and v for intervals I1 (solid line) and I2 (dashed line) of Subject B. We use the mean values and standard deviations from Fig. 4 to compute the percentage uncertainties. (a) Histogram values for f_0. (b) Histogram values for v. We express the histogram values as ratios

(a)

(b)
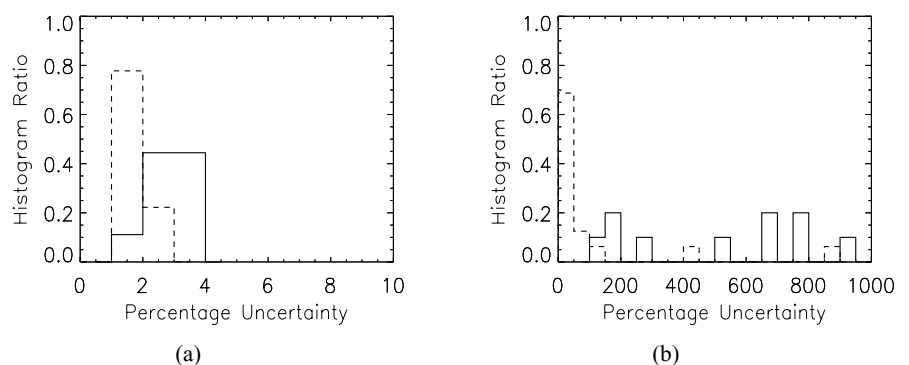
the WCC between each electrode of the 3×3 subgrid and its (three, five, or eight) neighbors. We follow the procedure discussed in *Methods* and show the results for v in I1 and I2 in Figs. 4(a) and (b), respectively. Here we plot an arrow connecting each electrode—denoted by a circle of radius f_0—with its neighbors if the uncertainty in v is less than ten times the magnitude of v between the two electrodes. For example, in Fig. 4(a) we do not draw an arrow between the electrode in the lower left corner and its neighbor to the right; for this electrode pair, we find $v = 3 \pm 96$ m/s, and $96 > 3 \times 10 = 30$. When an arrow is drawn, we indicate the direction of v with an arrowhead and write the mean value of v and its standard deviation along the line segment. If the mean value of v exceeds one standard deviation from zero, we draw the line segment solid and the arrowhead filled. Otherwise, we draw the line segment dashed and the arrowhead unfilled. There are 10 dashed arrows in Fig. 4(a), and 13 solid and 3 dashed arrows in Fig. 4(b). We note that the uncertainty in the mean—expressed as a percentage—tends to be larger for v in I1 than in I2 (i.e., we draw only dashed arrows in Fig. 4(a) and mostly solid arrows in Fig. 4(b)). To illustrate this we plot in Fig. 5(b) a histogram of the percentage uncertainties in v shown in Fig 4(a) for intervals I1 (solid line) and I2 (dashed line). Here we only consider percentage uncertainties less than 1000%; we omit results with larger uncertainties from Fig. 4(a). In I2 the percentage uncertainty tends to be less than 200%; in I1 the percentage uncertainty tends to be greater than 200%. We interpret this result to suggest that the variability in v typically decreases during the course of a seizure. Below we compare these results for v with those from the mathematical model.

We find for Subject B that the magnitudes of v shown in Fig. 4(a) range from near 0.3 m/s to 2.4 m/s, with a maximum uncertainty in the mean of 10.2 m/s; and shown in Fig. 4(b) range from 0.4 m/s to 9.0 m/s, with a maximum uncertainty in the mean of 79.1 m/s. For most electrode pairs, the magnitudes of the observational results agree with those determined from the model (v near 2 m/s) within a factor of four, although we note the large uncertainties in the means. An inspection of Fig. 4(b) reveals an approximate motion of the wave from the upper left corner to the lower right corner. This motion is not apparent during the first interval I1 shown in Fig. 4(a).

Subject C

To investigate the seizing activity recorded on the electrode grid of Subject C, we consider a 3×3 subgrid of electrodes situated on the lateral aspects of the anterior to left temporal lobe. We repeat the analysis performed for Subject B to compute f_0 and v for Subject C. For each of the nine electrodes, we compute the WPS, and determine the average frequency of maximum power during the seizing interval. We repeat this analysis for three of the subject's seizures (we were unable to extract the data for the other three seizures) and average the results over the seizures to compute f_0 in intervals I1 and I2. We show the results for f_0 from the 3×3 subgrid in Fig. 6. We illustrate the f_0 results by following the plotting scheme we used to create Fig. 4. We find that for Subject C the values of f_0 in I1 range from 8.8 Hz to 12.5 Hz, with a maximum uncertainty in the mean of 0.7 Hz, and for f_0 in I2 from 7.3 Hz to 9.0 Hz with a maximum uncertainty
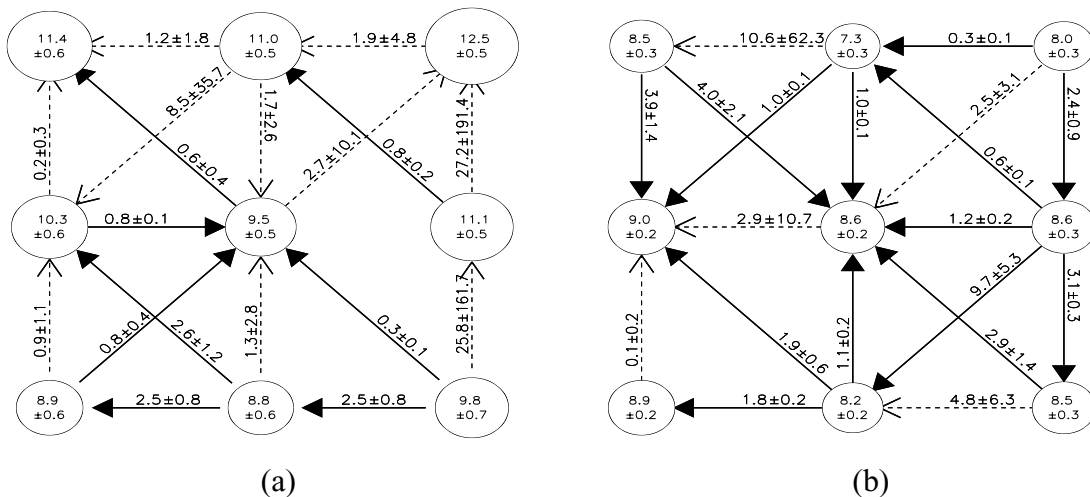
Fig. 6 Results for f_0 and v from Subject C recorded from the 3×3 electrode subgrid. The radius of each circle corresponds to the mean value of f_0 at the electrode. We write the mean and uncertainty in f_0 (in Hz) within each circle. The arrows indicate the value and uncertainty of v between neighboring electrodes. If the uncertainty in v is less than ten times the magnitude of v, then we draw an arrow connecting the two electrodes. We indicate the direction of v with the arrow and write the mean value of v and its standard deviation along the line segment. If the mean value of v exceeds one standard deviation from zero, then we draw the line segment solid and the arrowhead filled. Otherwise, we draw the line segment dashed and the arrowhead unfilled. (a) f_0 and v in I1. (b) f_0 and v in I2

Fig. 7 Histograms of the percentage uncertainty in f_0 and v for intervals I1 (solid line) and I2 (dashed line) of Subject C. We use the mean values and standard deviations from Fig. 6 to compute the percentage uncertainties. (a) Histogram of the uncertainty in f_0. (b) Histogram of the uncertainty in v. We express the histogram values as ratios
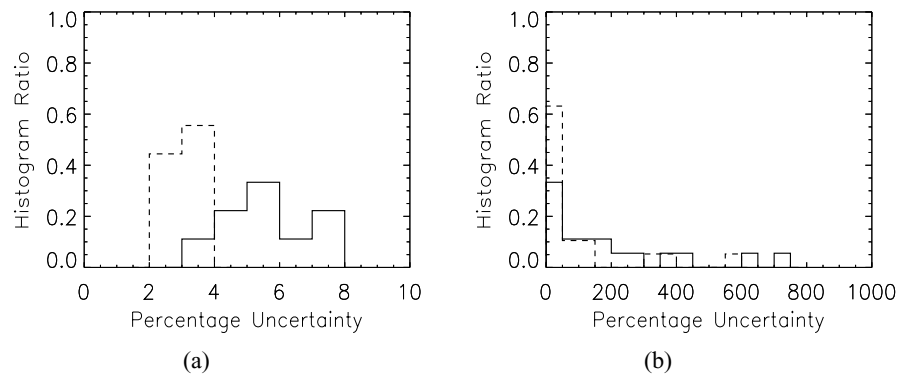
in the mean of 0.3 Hz, in agreement with the model results (f_0 near 10 Hz) within a factor of two. We note that the mean value and variability (shown as a histogram of percentage uncertainties in Fig. 7(a)) of f_0 in I1 tend to exceed that in I2. We compare these results with the mathematical model below.

To determine v we follow the procedure described for Subject B. We show the results for v in I1 and I2 from Subject C in Figs. 6(a) and (b), respectively. The plotting scheme follows that used to create Fig. 4. As in Fig. 4, we draw arrows only between those neighboring electrodes whose uncertainty in v is less than ten times the magnitude of v. We indicate the direction of v with an arrowhead and write the mean value of v and its standard deviation along the line segment. If the mean value of v exceeds one standard deviation from zero, we draw the line segment solid and the arrowhead filled. Otherwise, we draw the line segment dashed and the arrowhead unfilled. There are 8 solid and 10 dashed arrows in Fig. 6(a) and 14 solid and 5 dashed arrows in Fig. 6(b). As for Subject B, we note that the uncertainty in the mean—expressed as a percentage—tends to be larger in I1 than in I2. To illustrate this, we plot in Fig. 7(b) a histogram of the percentage uncertainty. In this case, we find that the distribution for I2 is more sharply peaked near zero than that for I1, although this difference is weak.

We find that the magnitudes of v range from 0.2 m/s to 27.2 m/s with a maximum uncertainty in the mean of 191.4 m/s in I1, and from 0.1 m/s to 10.6 m/s with a maximum uncertainty in the mean of 62.3 m/s. In most cases, the magnitudes of v agree with those calculated from the model calculations (v near 2 m/s) within a factor of ten. An inspection of Fig. 6(b) reveals an approximate propagation of the waves to the center of the subgrid. This propagation is not apparent during the interval I1 shown in Fig. 6(a).

Comparison of observational and model results

In the previous three subsections we computed two quantities (f_0 and v) from ictal ECoG data recorded from three human subjects. We compared these results with identical quanti-

ties computed from a mathematical model of human cortical electrical activity. The model—stated in *Methods*—consists of a system of SPDEs with solutions that can exhibit wave propagation suggestive of a seizure when we alter two parameters (P_{ee} and Γ_e) that affect the excitation of the model cortex. We found that the simulated and observed results for f_0 and v agreed during seizures. We have also found that the characteristics of the ECoG data change during the course of the seizure. To determine a crude measure of this change, we divided the ECoG data into two temporal intervals and computed f_0 and v in each. We found that, for two subjects (Subject A and Subject C), f_0 in I1 typically exceeded f_0 in I2 (this relationship held for two electrodes of Subject B). We also found that the observed variability in f_0 and v tends to be larger in I1 than in I2 for Subject B and Subject C. We use these observations to deduce two qualitative conclusions: (1) the frequency of maximum power, and (2) variability in the velocity of propagation and frequency of maximum power tend to decrease during the course of a seizure.

We now suggest that both qualitative results are consistent with the mathematical model. We first consider (1): that f_0 tends to decrease during the course of a seizure. To change the frequency of maximum power in the mathematical model, we adjust the two parameters P_{ee} and Γ_e. We show the dependence of the dominant oscillation frequency of h_e on P_{ee} and Γ_e in Fig. 8. To create this figure, we follow the procedure in Kramer et al. (2005) and Kramer et al. (2006) and compute numerical solutions to a simplified model: the dimensionless ordinary differential equations (ODEs). The ODEs differ from the SPDEs in two ways. First, the ODEs lack stochastic input. Second, the ODEs lack spatial dependence; it is a perhaps helpful oversimplification to think of the ODEs as modeling ECoG data recorded at a single electrode. We define a "seizure" as a solution to the ODEs for which h_e undergoes large amplitude, stable oscillations (Kramer et al., 2005). We compute numerical solutions to the ODEs for $11.0 < P_{ee} < 1000.0$ and $0.4 \times 10^{-3} < \Gamma_e < 1.5 \times 10^{-3}$ using a fourth-order Runge–Kutta method with a time step of 0.4 ms. For each solution, we calculate the power spectrum of h_e after transient behavior
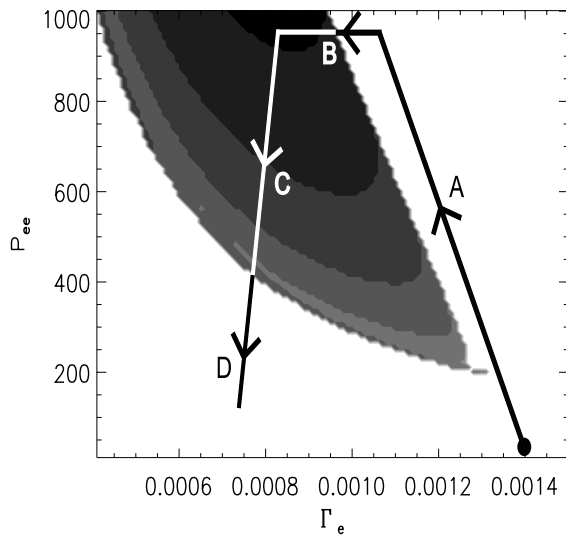
Fig. 8 The frequency of oscillations in h_e for solutions of the ODEs model as a function of parameters P_{ee} (vertical axis) and Γ_e (horizontal axis). The frequency is plotted in linear greyscale with white representing 0 Hz (no oscillations) and black representing 10 Hz and larger. We indicate the typical values of P_{ee} and Γ_e with a solid circle in the lower right corner of the figure, and draw a trajectory—consisting of four arrows labeled A, B, C, and D—suggestive of how seizures might evolve in the model

has decayed and determine the frequency of maximum power. We note that the frequency resolution of this calculation is 0.5 Hz, and that the power spectra possess a single, well-defined peak. We show the results of this calculation in Fig. 8. Here we use to white represent parameter regions without oscillations in h_e (i.e., fixed points), and a linear greyscale to indicate the dominant frequency of oscillation in h_e; black represents oscillations with frequency greater than 10 Hz and the lightest gray represents oscillations with frequency less than 2 Hz. We note that, to induce seizure-like oscillations in the model, we must decrease the typical value of Γ_e by at least 12%, and increase the typical value of P_{ee} by at least 2200%. We indicate the typical parameter values with a solid black circle in the figure.

We use the results shown in Fig. 8 to speculate how parameters P_{ee} and Γ_e might evolve to produce a seizure. We start at the typical parameter values $(\Gamma_e, P_{ee}) = (1.4 \times 10^{-3}, 11.0)$—the solid circle. We then decease Γ_e by a small amount and increase P_{ee} by a large amount without invoking a seizure. We indicate this initial trajectory with an arrow emanating from the default parameter values and with label A. The seizure initiates when we adjust the parameters (here decrease Γ_e) to enter the shaded region (trajectory B). At this point, h_e undergoes large amplitude, stable oscillations at a dominant frequency greater than 10 Hz. These seizure-like oscillations persist at lower frequencies as we decrease P_{ee} and Γ_e along trajectory C; this trajectory begins at the dark shaded region (high frequency oscillations) and ends at

the lighter shaded region (low frequency oscillations). The physiological motivation for the decrease in P_{ee} and Γ_e may be, say, exhaustion of excitatory subcortical input or AMPA (affecting the *dimensional* parameter G_e and thus Γ_e—see Table 2), respectively. The seizure halts as these physiological mechanisms continue and we adjust P_{ee} and Γ_e to exit the shaded region (trajectory D). The parameters might then return to the typical values (the filled circle) and the cycle repeat. This putative trajectory in the (Γ_e, P_{ee}) plane provides an example of how seizures might initiate (trajectory B), decrease in dominant frequency (trajectory C), and terminate (trajectory D) in qualitative agreement with the observational f_0 results.

We may also adjust the model parameters to account for the second observed qualitative result: the decreased variability in f_0 and v during the course of a seizure. To do so, we consider the complete SPDE model in (1). We compute two numerical solutions to the model using the Euler-Maruyama algorithm with fixed steps in space and time, 14 mm and 0.1 ms, respectively, and periodic boundary conditions in space. Here we consider the dynamics in one spatial dimension and set all parameters at the typical values except for: $\Gamma_e = 0.8 \times 10^{-3}$ (a decrease in the typical value by 40%), the stochastic input (set so that the variance at a fixed point of h_e is approximately 3 mV), and P_{ee}. In both simulations, we fix P_{ee} to be Gaussian in space with center at $x = 350$ mm, a minimum value of 11.0, a maximum value of P_{ee}^0, and a half-width of x_{HW}. We adjust P_{ee}^0 and x_{HW} so that the Gaussian distributions possess different peaks and widths. We employ this change in P_{ee} as a crude speculation of how the excitatory subcortical input to the seizing cortex might evolve during the course of a seizure.

We show the results of the two simulations in Fig. 9. Here we plot (dimensional) space on the horizontal axis, (dimensional) time on the vertical axis, and the value of h_e in linear greyscale; white corresponds to $h_e = -100$ mV, and black to $h_e = 0$ mV. To create Fig. 9(a) we set $P_{ee}^0 = 1000.0$ and $x_{HW} = 56$ mm. For reference, we plot the spatial distribution of P_{ee} as a thick, solid line in Fig. 9(a). Seizures—large amplitude oscillations in h_e represented by the alternating light and dark ridges—occur mainly in the spatially localized region of large P_{ee}. As a voltage wave propagates outward, it decays into the background activity. We may compare this simulation with the observational results by considering the dynamics of h_e at two fixed spatial locations, both near the edge of the seizing region. For example, consider h_e recorded at $x = 500$ mm and $x = 550$ mm. At both locations the traveling wave has decayed significantly and the oscillations are weak and sometimes do not occur. We may follow the procedure in *Methods* and use the WPS and WCC to compute f_0 and v, respectively. The large variability in the WPS and WCC—due to the inconsistent arrivals of traveling waves—results in larger variabilities in f_0 and v.
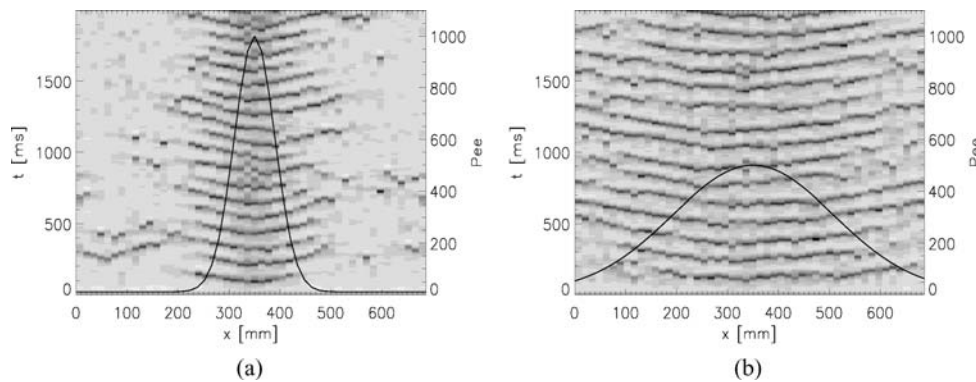
Fig. 9 Numerical solution to the SPDEs. We set P_{ee} Gaussian in space with center at $x = 350$ mm, a maximum value of P_{ee}^0, and a half-width of x_{HW}. Space (in mm) and time (in ms) are plotted along the horizontal and (left) vertical axes, respectively. The value of h_e is plotted in linear greyscale over space-time with $h_e = -100$ mV in white and $h_e = 0$ mV in black. We plot P_{ee} as a thick solid line and indicate its value on the right vertical axis. (a) $P_{ee}^0 = 1000.0$ and $x_{HW} = 56$ mm. (b) $P_{ee}^0 = 500.0$ and $x_{HW} = 224$ mm

In the second case, we set $P_{ee}^0 = 500.0$ and $x_{HW} = 224$ mm. We show P_{ee} in Fig. 9(b) as a thick solid line and note that, compared to the P_{ee} distribution in Fig. 9(a), this subcortical excitatory input is broader and weaker. In this case the seizure-like oscillations cover more of the one-dimensional surface. Here P_{ee} decays slowly and the oscillations propagate further from the distribution's center. If we use the WPS and WCC to compute f_0 and v at locations $x = 500$ mm and $x = 550$ mm, we find less variability in the results. In this case, traveling waves persists and the oscillations are robust at both locations. We note that the decrease in P_{ee} results in a decreased temporal oscillation frequency, as shown in Fig. 8 for the ODEs model.

In the observational data the variability in f_0 and v arose from two sources. First, for each seizure, we computed the WPS or WCC and averaged the frequency of maximum power or averaged the time lags of maximum correlation, respectively, over intervals I1 and I2. This averaging procedure produced an uncertainty in the result for each seizure. Second, we averaged these results over the seizures to compute f_0 and v. This averaging introduced a second source of variability in the observational results. We use the simulations above to suggest a mechanism for the first type of variability. We postulate that during interval I1 a strong, compact focus of cortical seizing activity exists so that the propagating waves quickly decay and large variability in f_0 and v result at most locations (as in Fig. 9(a)). Then, during interval I2, the region of seizing activity weakens and broadens so that the propagating waves travel further over the cortical surface and the variability in f_0 and v decrease at most locations (as in Fig. 9(b)).

Analysis of model parameters

Having found agreement between the observational and model results, we suggest that the SPDEs can approximate the electrical activity of the seizing human cortex. Therefore, in this subsection, we interpret the model results to determine what changes in cortical physiology might result in seizures. In Kramer et al. (2005) we computed numerical solutions to the ODEs and showed that seizures—large amplitude, stable oscillations in h_e—result from changes in two model parameters: an increase in P_{ee} and a decrease in Γ_e. We considered changes in these two parameters because both affect the excitation of the model cortex. In what follows, we now consider whether other parameter changes can result in seizure-like oscillations in h_e. To do so, we keep P_{ee} increased to nearly 50 times its typical value. Therefore, the excitatory cell populations still receive strong, subcortical excitatory input; we call this model cortex "hyper-excited." It is neurobiologically plausible that the "hyper-excited" state is a common initiating factor in seizures, because pre-ictal depolarization of the soma potential in neuronal populations is almost always observed as a precursor to seizure (Dzhala and Staley, 2003). We then vary those parameters affecting connectivity between cell populations (i.e., within and between the excitatory and inhibitory populations). To examine all types of connectivity, we relax several assumptions made in Kramer et al. (2005). In that work, we assumed that connections between neuronal populations were independent of the post-synaptic population. For example, in Kramer et al. (2005), we defined the parameter Γ_e as the influence of excitatory input on both excitatory and inhibitory postsynaptic cell populations. A change in Γ_e, therefore, affected excitatory and inhibitory populations equally. To enable exploration of more specific connectivity changes, we replace Γ_e with two parameters: Γ_{ee} and Γ_{ei}. The new parameter Γ_{ee} defines the influence of excitatory input on postsynaptic excitatory populations, and the new parameter Γ_{ei} defines the influence of excitatory input on postsynaptic inhibitory populations. We perform similar changes to three other model parameters (Γ_i, N_e^β, and N_i^β) that affect connectivity between neuronal

Table 4 Definitions of dimensionless parameters effecting connectivity between excitatory and inhibitory neural populations in the ODEs. The original parameters in the first column are from Kramer et al., (2005). We list the symbols for the new parameters in the second column and define these parameters in terms of dimensional components from Steyn-Ross et al. (2003), and in words in the third and forth columns, respectively. We write the typical value from Kramer et al. (2005) in the fifth column, and the percentage change in the typical parameter value necessary to induce seizure-like oscillations in the hyper-excited model cortex (i.e., $P_{ee} = 548.066$) in the last column

Old	New	Dims	Definition	Typical	Δ
Γ_e	Γ_{ee}	$\dfrac{G_{ee}\exp(1)S^{\max}}{\gamma_{ee}\lvert h_{ee}^{\text{rev}}-h_e^{\text{rest}}\rvert}$	influence of **excitatory** input on the mean soma membrane values of **excitatory** neurons	1.42×10^{-3}	-12%
	Γ_{ei}	$\dfrac{G_{ei}\exp(1)S^{\max}}{\gamma_{ei}\lvert h_{ei}^{\text{rev}}-h_i^{\text{rest}}\rvert}$	influence of **excitatory** input on the mean soma membrane values of **inhibitory** neurons	1.42×10^{-3}	$+28\%$
Γ_i	Γ_{ie}	$\dfrac{G_{ie}\exp(1)S^{\max}}{\gamma_{ie}\lvert h_{ie}^{\text{rev}}-h_e^{\text{rest}}\rvert}$	influence of **inhibitory** input on the mean soma membrane values of **excitatory** neurons	0.0774	$+14\%$
	Γ_{ii}	$\dfrac{G_{ii}\exp(1)S^{\max}}{\gamma_{ii}\lvert h_{ii}^{\text{rev}}-h_i^{\text{rest}}\rvert}$	influence of **inhibitory** input on the mean soma membrane values of **inhibitory** neurons	0.0774	-22%
N_e^β	N_{ee}^β	–	number of local **excitatory** synapses on **excitatory** neurons	3034	-28%
	N_{ei}^β	–	number of local **excitatory** synapses on **inhibitory** neurons	3034	$+39\%$
N_i^β	N_{ie}^β	–	number of local **inhibitory** synapses on **excitatory** neurons	536	$+12\%$
	N_{ii}^β	–	number of local **inhibitory** synapses on **inhibitory** neurons	536	-19%

populations. We define the eight new parameters and list the typical values in the second and fifth columns of Table 4, respectively.

Having established the validity of the model and defined the eight new parameters, we now determine which parameter changes result in seizure-like oscillations in the dynamics. To do so, we fix seven of the new parameters at the typical values, change one parameter by a small amount, and compute a numerical solution to the ODEs. We compute the numerical solutions here, and in what follows, using a forth-order Runge-Kutta method with time step of 0.4 ms. We find that the variable h_e—the observable variable we compare to the ECoG data—either approaches a steady state value, or undergoes large amplitude oscillations. If h_e approaches a steady state value, we change the same parameter by a small amount and compute another numerical solution to the ODEs. We continue this procedure until the parameter becomes implausible (e.g., negative) or h_e undergoes oscillations. If a small change in the parameter results in oscillations in h_e, then we say that this parameter induces a seizure in the model. In the last column of Table 4, we list the percentage change in each parameter necessary to induce seizure-like oscillations in h_e.

We illustrate the results of this analysis in Fig. 10. In this figure, we show a schematic of the mathematical model (Kramer et al., 2005). The eight rectangular boxes represent the 8 model (dimensionless) variables ($\tilde{h}_e$, $\tilde{h}_i$, $\tilde{I}_{ee}$, $\tilde{I}_{ei}$, $\tilde{I}_{ie}$, $\tilde{I}_{ii}$, $\tilde{\phi}_e$, and $\tilde{\phi}_i$) we define in Table 1. We again note that the dimensional variable h_e is related to the dimensionless variable $\tilde{h}_e$ by a simple scaling: $h_e = -70\,\text{mV}\times\tilde{h}_e$. The arrows represent connections between the variables, and between variables and subcortical inputs (P_{ee}, P_{ei}, P_{ie}, and P_{ii} at
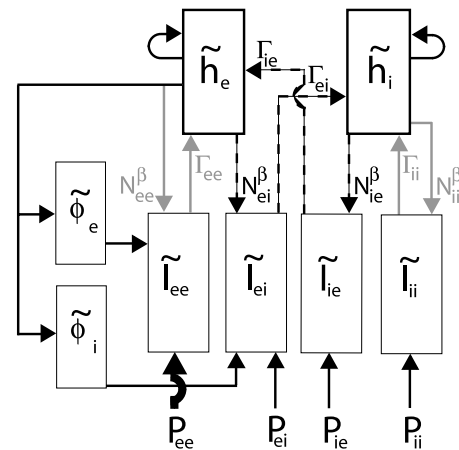
Fig. 10 A schematic representation of the connections between the 8 (dimensionless) variables ($\tilde{h}_e$, $\tilde{h}_i$, $\tilde{I}_{ee}$, $\tilde{I}_{ei}$, $\tilde{I}_{ie}$, $\tilde{I}_{ii}$, $\tilde{\phi}_e$, and $\tilde{\phi}_i$) and the 4 subcortical inputs (P_{ee}, P_{ei}, P_{ie}, P_{ii}) in the model. We indicate the interactions between the variables using arrows and label the eight connections that affect the connectivity within and between the excitatory and inhibitory cell populations. We have increased P_{ee} by nearly a factor of 50; we denote this increase with the thick, solid arrow. To induce seizures in the hyper-excited model dynamics, we may increase the strength of any single one of the black, dashed connections or decrease the strength of any single one of the grey, solid connections by the amounts shown in Table 4

the bottom of the figure). Because we have increased P_{ee} by nearly 5000%, we draw a thick arrow connecting it to $\tilde{I}_{ee}$. To make the model "seize" we change the parameters listed in the second column of Table 4 one at a time. We label the connections affected by each of these parameters in the figure. For example, to alter the strength of connection from $\tilde{h}_e$ to $\tilde{I}_{ee}$ we change the parameter N_{ee}^β. We find that seizure-like oscillations result in $\tilde{h}_e$ (or h_e) when we

decrease N_{ee}^{β} by 28%. We indicate that a decrease in N_{ee}^{β} results in a seizure by shading the arrow and label for this connection in grey. We find that the model dynamics "seize" as we increase or decrease each of the eight parameters. We indicate the direction of change in Fig. 10; we find that seizure-like oscillations results in h_e when we increase the strength of the connections drawn in black and with dashed lines, or decrease the strength of the connections drawn in grey and with solid lines. We note that seizures result in the model from an increased connectivity between the two cell populations (i.e., between the excitatory and inhibitory populations), and a decreased connectivity within each population (i.e., within the excitatory population or within the inhibitory population).

So far we have discussed how to make the model "seize" by changing the *dimensionless* parameters listed in the second column of Table 4. We now discuss the relationship between these parameter changes in the model and physiological changes in the cortex. To do so, we first define each dimensionless parameter in terms of *dimensional* quantities as in Kramer et al. (2005). We list these definitions in the third column of Table 4. We note that the four parameters N_{ee}^{β}, N_{ei}^{β}, N_{ie}^{β}, and N_{ii}^{β} have no dimensional counterparts; each of these parameters represents a true dimensionless quantity: the mean number of synapses.

The dimensional definitions of Γ_{ee}, Γ_{ei}, Γ_{ie}, and Γ_{ii} are more complicated. Each contains four quantities: G_{jk}, γ_{jk}, h_{jk}^{rev}, and h_k^{rest}; where $j \in \{e, i\}$ and $k \in \{e, i\}$; as well as $S^{\max}$ and the exponential $\exp(1)$. To allow more types of connectivity than what we considered in Kramer et al. (2005) we again assume that the parameters depend upon the postsynaptic cell population (i.e., the values differ for synapses terminating on an excitatory or inhibitory postsynaptic cell). For example, we define the neurotransmitter rate constants γ_{jk} with two subscripts. The first (j) defines the presynaptic neuron and the second (k) defines the postsynaptic neuron. Other researchers who investigate the SPDEs model do not make this assumption (Steyn-Ross et al., 2003). We allow this parameter (as well as the parameters G_{jk}, N_{jk}^{β}, h_k^{rest}, and h_{jk}^{rev}) dependence on the postsynaptic neuron to explore more specific behavior in the model; we assume that the cell resting potential h_k^{rest} depends only on the postsynaptic neuron k. A change in a dimensionless parameter can result from a change in any of the dimensional parameters of which it is comprised. For example, to decrease the dimensionless parameter Γ_{ee} and induce seizure-like oscillations in the model dynamics, we can: decrease G_{ee} or $S^{\max}$, or increase γ_{ee} or the difference $|h_{ee}^{\text{rev}} - h_e^{\text{rest}}|$. We list these dimensional quantities, their definitions, and the direction of change necessary to produce seizing dynamics in the model in Table 5. We include the parameters N_{ee}^{β}, N_{ei}^{β}, N_{ie}^{β}, and N_{ii}^{β} in this table, although these parameters are dimensionless.
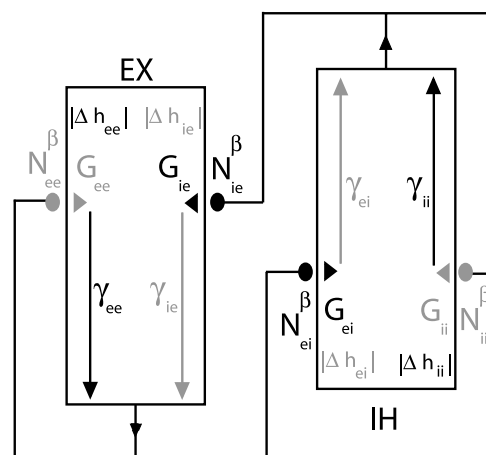
Fig. 11 A cartoon of two interconnected neuronal populations (excitatory—EX—on the left and inhibitory—IH—on the right) and 16 physiological parameters. The filled circles denote synapses (N^{β}_{jk}), the triangles denote peak amplitudes of the postsynaptic potentials (G_{jk}), and the vertical arrows within EX and IH denote the rate constants (γ_{jk}). We also indicate the voltage difference between the reversal and resting potential by the label $|\Delta h_{jk}|$. To induce seizure-like oscillations in the model dynamics, we must either increase any one of the black parameters or decrease any one of the grey parameters

We illustrate the changes in the dimensional quantities listed in Table 5 in Fig. 11. We show in this figure a cartoon representation of the local connections between the two cell populations. (By local connections we mean connections established within a small spatial neighborhood, not long-range, corticocortical connections). We draw the excitatory and inhibitory populations as rectangles on the left and right of Fig. 11, respectively. The populations establish feedback and reciprocal synaptic connections. We draw these connections leaving the bottom of the excitatory population and the top of the inhibitory population. We illustrate the number and strength of the synapses formed by each connection with a filled circle labeled N_{jk}^{β} and a filled triangle labeled G_{jk}, respectively. Inside the rectangular label for each population we show the rate constants γ_{jk} with vertical arrows and the voltage differences $|h_{jk}^{\text{rev}} - h_k^{\text{rest}}| \equiv |\Delta h_{jk}|$ in text. The rate constants incorporate the time course of somatically recorded postsynaptic spike activity in a neuron due to the combined effects of passive dendritic cable delays and neurotransmitter kinetics, such as excitatory AMPA and inhibitory GABA (Liley et al., 2002). The voltage differences scale the synaptic input by the reciprocal of the magnitude difference between the reversal and resting potentials. We shade the labels for N_{jk}^{β}, G_{jk}, and γ_{jk}, and the text $|\Delta h_{jk}|$ to indicate changes in each quantity that result in seizing dynamics. To induce a seizure in the model dynamics we may increase the dimensional parameters drawn in black or decrease the dimensional parameters drawn in grey.

Table 5 Definitions of dimensional parameters from Kramer et al. (2005) effecting connectivity between excitatory and inhibitory neural populations in the ODEs. We define each parameter in words in the second column. We indicate the direction of change in each parameter necessary to induce seizure-like oscillations in the hyper-excited model cortex (i.e., $P_{ee} = 548.066$) in the last column. Here PSP stands for postsynaptic potential, EPSP for excitatory postsynaptic potential, and IPSP for inhibitory postsynaptic potential

Parameter	Definition	Δ for seizure
$G_{ei,ie}$	mean peak amplitude of the PSP induced by a single presynaptic spike from an (excitatory, inhibitory) neuron at the synapses of an (inhibitory, excitatory) postsynaptic neuron	$\uparrow$
$G_{ee,ii}$	mean peak amplitude of the PSP induced by a single presynaptic spike from an (excitatory, inhibitory) neuron at the synapses of an (excitatory, inhibitory) postsynaptic neuron	$\downarrow$
$N^{\beta}_{ei,ie}$	the number of local (excitatory, inhibitory) synapses on (inhibitory, excitatory) neurons	$\uparrow$
$N^{\beta}_{ee,ii}$	the number of local (excitatory, inhibitory) synapses on (excitatory, inhibitory) neurons	$\downarrow$
$\gamma_{ee,ii}$	the neurotransmitter rate constant for (EPSPs, IPSPs) to travel from the dendrites to the soma of an (excitatory, inhibitory) neuron	$\uparrow$
$\gamma_{ei,ie}$	the neurotransmitter rate constant for (EPSPs, IPSPs) to travel from the dendrites to the soma of an (inhibitory, excitatory) neuron	$\downarrow$
$|h^{rev}_{ee,ii} - h^{rest}_{e,i}|$	the difference between the reversal potential associated with (excitatory, inhibitory) synaptic activity on (excitatory, inhibitory) cells and the (excitatory, inhibitory) cell rest potential	$\uparrow$
$|h^{rev}_{ei,ie} - h^{rest}_{i,e}|$	the difference between the reversal potential associated with (excitatory, inhibitory) synaptic activity on (inhibitory, excitatory) cells and the (inhibitory, excitatory) cell rest potential	$\downarrow$
S^{max}	the maximum value of the sigmoid transfer function that maps the soma voltage to average output spike rate	$\uparrow \downarrow$

Discussion

In *Results* we computed two quantities (f_0 and v) from ictal ECoG data recorded from three human subjects. We compared these results with identical quantities computed from a mathematical model of human cortical electrical activity, stated in *Methods*, and found that the simulated and observed results agreed in two ways during seizures: f_0—the frequency of maximum power, and v—the speed of voltage propagation. We note that the speed of voltage propagation (near 2 m/s) is similar to the velocity of axonal conduction in cortical white matter (variously reported as 0.5–5 m/s). Other investigators have observed propagation of seizure activity at these velocities in intact brains, particularly in cross callosal spread (Gotman, 2003). In contrast, seizure activity in slice preparations—which have minimal white matter connections—spreads several orders of magnitude more slowly (only about 1 mm/s) (Weissinger et al., 2005). This hints that white-matter conduction—rather than local cortical grey-matter spread—may be an important mechanism in seizure propagation (Sutherling and Barth, 1989; Nowak et al., 1997).

We also found that the characteristics of the ECoG data changed during the course of a seizure. We characterized these changes by dividing the observational data into two temporal intervals and computing f_0 and v in each. From this we deduced two qualitative conclusions: (1) the frequency of maximum power, and (2) the variability in the velocity of propagation and frequency of maximum power tended to decrease during the course of a seizure. In *Results* we suggested how parameters P_{ee} and Γ_e might evolve to produce similar qualitative results in the model. Namely, we showed that a decrease in f_0 and decreases in the variability of f_0 and v may result from large temporal changes and spatial broadening of P_{ee} and small temporal changes in Γ_e. Both parameter changes could plausibly be caused by a variety of physiological mechanisms (e.g., changes in the resting potential of both neural populations, the neurotransmitter rate constant, the maximum firing rate, and/or the synaptic gain).

Finally we studied parameter changes in the simplified ODEs model. We defined eight dimensionless parameters affecting the connectivity between the excitatory and inhibitory cell populations and found that seizure-like oscillations can result from changes in each. We used these results to suggest two methods for inducing seizure-like oscillations in the ODEs. First, we may increase the (dimensionless) strength of connections between the excitatory and inhibitory cell populations (the inter-population connectivity). We illustrated these connections in Fig. 10 with black, dashed lines. Second, we may decrease the (dimensionless) strength of connections within the excitatory cell population or within the inhibitory cell population (the intra-population connectiv-

ity). We illustrated these connections with grey, solid lines in Fig. 10. We concluded that strong interactions between the excitatory and inhibitory cell populations result in seizure-like oscillations in the model dynamics.

To allow an easier comparison of the model results with cortical physiology, we defined each dimensionless parameter in terms of its dimensional components. We listed these definitions in the third column of Table 4. Because both increases and decreases in the dimensional parameter $S^{\max}$ result in seizure-like oscillations, we do not consider this parameter further. We illustrated the results for the dimensional parameters in Fig. 11. We found that seizure-like oscillations can result from both increases (shown in black) or decreases (shown in grey) in the model parameters and summarized these results in Table 5.

The novel result from the model is the suggestion that the balance of intra-population ($e \rightarrow e$ and $i \rightarrow i$) versus inter-population ($e \rightarrow i$ and $i \rightarrow e$) connectivity is an important mechanism in the causation (or propagation) of seizures in the hyper-excited cortex. From this two questions arise: what physiological homeostatic (self-organizing) mechanisms are present in the nervous system to maintain this balance in health, and thus prevent seizures? And, what biological or pharmacological effects could cause a neuronal population imbalance of 10%–40%, thus making the cortex vulnerable to convulsions? There is not much experimental work reported in the literature that explicitly, and quantitatively, describes such imbalances but we will compare predictions from the model with some reported data. In doing so we shall attempt—perhaps naively and on purely theoretical grounds—to connect tentatively these agents or mechanisms with the foregoing discussion of our mathematical model. The value of such an undertaking at this early stage of model development is in clarifying thoughts about the mechanism of action of drugs or pathological states and their relationship to our model. A more robust analysis may prove or disprove these relationships, and perhaps suggest new parameters required in the model.

First we mention that various neurological diseases or trauma have pathological effects at the anatomic/neuronal scale. These could be modeled as imbalances in N_{ee}^{β} and N_{ie}^{β}. It would be easy to imagine imbalances in N_{ee}^{β} and N_{ie}^{β} occurring in neuronal scar tissue. Neuronal loss and gliosis are characteristic of tissue in which seizures arise, and indeed this pathological effect is used to increase the propensity for convulsions in several experimental animal models of epilepsy (e.g., (Dichter, 2006)).

Second, there are numerous different types of inhibitory neuron with specific anatomical connections to different cell types. For example the so-called "chandelier" and "basket" interneurons target the axonal segments of the pyramidal cells—and thus would form an important part of the inhibitory to excitatory connectivity in our model (Krimer

et al., 2005). It has been postulated that inactivity, disconnection, or deficiency of these (inhibitory-onto-excitatory) chandelier and basket interneurons may allow uncontrolled excitatory activity and hence seizures—the so-called disinhibition hypotheses of seizure causation (for a critical review, see (Bernard et al., 1998)). Inactivity of basket cells in the CA1 of the rat hippocampus has been called the dormant basket cell hypothesis (Bekenstein and Lothman, 1993). Similarly, a deficiency of chandelier cells has also been proposed as a cause of seizures (DeFelipe, 1999). However recent work suggests that this hypothesis is over-simplified (Arellano et al., 2004), and that the converse may be true. There is experimental evidence that seizure activity is associated with strong firing of chandelier cells, and a strong positive feedback circuit between the pyramidal cells and the chandelier inhibitory neurons (Fujiwara-Tsukamoto et al., 2004). This is precisely the pattern of activity that is predicted by our model. Although our mathematical model describes cortical seizure propagation—*not* hippocampal seizure genesis—the relative effects of disinhibition-induced hyper-excitability versus intra-population and inter-population connectivity clearly need more detailed quantitative experimental investigation.

We may also use the model to understand pharmacological induction, or suppression, of seizures. To do this we must consider the effects of drugs acting on receptor molecules (usually proteins). There are typically many subtypes of these receptors, which are heterogeneously distributed between different populations of neurons. It must be acknowledged that many drug effects are erratic and context-dependent. The same drugs that induce seizures may also treat seizures, and antiepileptic drugs are occasionally proconvulsant. We would speculate that this phenomenon could be the result of subtle differences in the action of the drugs on different receptor subtypes which are present on different, interconnected neuronal populations.

In experimental preparations the proconvulsant 4-aminopyridine (4-AP) is commonly used to generate seizures. The effects of 4-AP include enhancement of both excitatory and inhibitory synaptic transmission, perhaps by enhanced neurotransmitter release at the presynaptic cells (Rutecki et al., 1987), or leak potassium channel closure (Netoff and Schiff, 2002). The end result is an increased connectivity within the cell network. We relate these physiological changes to changes in the model parameters that increase the network connectivity, namely: an increase in G_{jk}—the mean peak amplitude of the postsynaptic potential induced by a presynaptic population j on postsynaptic population k—or N_{jk}^{β}—the number of local synapses from presynaptic population j to postsynaptic population k. We have found in model simulations that seizures result from relatively increased inter-population connectivity (i.e., increases in G_{ei}, G_{ie}, N_{ei}^{β}, and N_{ie}^{β}) and decreased intra-population

connectivity (i.e., decreases in G_{ee}, G_{ii}, N_{ee}^{β}, and N_{ii}^{β}). This would be supported by the 4-AP model if 4-AP acts to increase inter-population connectivity more strongly than intra-population connectivity.

We have shown how to induce seizure-like oscillations in the ODEs and how these model results compare to other proposed seizure mechanisms. We may also apply the analysis to suggest epilepsy treatments. We note that to *prevent* a seizure from occurring in the model dynamics, we may decrease the strength of the black, dashed connections (the inter-population connectivity) or increase the strength of the grey, solid connections (the intra-population connectivity) shown in Fig. 10. These changes correspond to a decrease in the black (dimensional) parameters or an increase in the grey (dimensional) parameters of Fig. 11.

We find that changes in many dimensional parameters (G_{jk}, N_{jk}^{β}, γ_{jk}, h_k^{rest}, and h_{jk}^{rest}) may prevent seizures in the model dynamics. This result may be useful in the development of medications to which patients do not develop tolerances. For example, one might develop treatments that target different physiological parameters (and different pathways in Fig. 11) so as not to exploit and perhaps desensitize any single pathway in particular.

To suggest how these preventative mechanisms determined from the model may relate to experimental results, we consider benzodiazepines (BZ). BZ are an important class of anticonvulsant drugs that act to enhance the action of GABA at GABA$_A$ receptors. We follow (Liley et al., 2002) and assume that the effect of BZ are to increase the model parameters G_{ie} or G_{ii}—the mean peak IPSP induced on excitatory and inhibitory postsynaptic cells, respectively. We have shown that an increase of G_{ie} *induces* seizure-like oscillations in the model dynamics. The observed anticonvulsant effects of BZ would be consistent with the model if it acts to increase G_{ii} rather than G_{ie}—perhaps mediated by differing distributions of GABA receptor subtypes on different classes of neurons. Once we know which receptor subtypes are present on a specific neuronal population (for example the ($i \to e$) basket cells), we may be able to design a specific GABA agonist that will act more strongly on other ($i \to i$) connections, but is less active (or even antagonistic) at the basket cell ($i \to e$) synapses. Analysis of the relationships between anticonvulsant medications and model parameters may eventually suggest how these drugs produce their therapeutic effects.

We conclude by noting two issues concerning our analysis. First, the electrode separation of 10 mm in the ECoG recordings may be too large to capture voltage propagation. To determine the properties of voltage propagation more accurately, one would like to use an electrode strip or grid with smaller inter-electrode distances. Smaller electrode spacing might also help ensure that neighboring electrodes are true

neighbors (and not separated by a sulcus, for example). Second, in comparing the observational and simulated results, we make an important assumption about the mathematical model. Namely, we set the parameter P_{ee} to 50 times its typical value (to "hyper-excite" the model cortex). Of course this assumption may be incorrect. Moreover, the ODEs model (and the complete SPDEs model) provides only a crude approximation to the true dynamics of the seizing cortex. Although simple, we find the model useful in making our assumptions explicit.

References

Arellano JI, Munoz A, Ballesteros-Yanez I, Sola RG, DeFelipe J (2004) Histopathology and reorganization of chandelier cells in the human epileptic sclerotic hippocampus. Brain. 127: 45–64.

Bekenstein JW, Lothman EW (1993) Dormancy of inhibitory interneurons in a model of temporal lobe epilepsy. Science. 259: 97–100.

Bernard C, Esclapez M, Hirsch J, Ben-Ari Y (1998) Interneurones are not so dormant in temporal lobe epilepsy: A critical reappraisal of the dormant basket cell hypothesis. Epilepsy Res. 32: 93–103.

DeFelipe J (1999) Chandelier cells and epilepsy. Brain. 122: 1807–1822.

Dichter MA (2006) Models of epileptogenesis in adult animals available for antiepileptogenesis drug screening. Epilepsy Res. 68: 31–35.

Dzhala VI, Staley KJ (2003) Transition from interictal to ictal activity in limbic networks in vitro. J. Neurosci. 23: 7873–7880.

Freeman WJ (1964) A linear distributed feedback model for prepyriform cortex. Exp. Neurol. 10: 525–547.

Fujiwara-Tsukamoto Y, Isomura Y, Kaneda K, Takada M (2004) Synaptic interactions between pyramidal cells and interneurone subtypes during seizure-like activity in the rat hippocampus. J. Physiol. 557: 961–979.

Gotman J (2003) Noninvasive methods for evaluating the localization and propagation of epileptic activity. Epilepsia. 44: 21–29.

http://www.epilepsyfoundation.org/ (2005) Epilepsy: An introduction

Kramer MA (2005) Nonlinear dynamics and neural systems: synchronization and modeling. Doctoral dissertation, University of California, Berkeley

Kramer MA, Kirsch HE, Szeri AJ (2005) Pathological pattern formation and cortical propagation of epileptic seizures. J. R. Soc. Interface. 2: 113–127.

Kramer MA, Lopour BA, Kirsch HE, Szeri AJ (2006) Bifurcation control of a seizing human cortex. Phys. Rev. E. 73: 041928.

Krimer LS, Zaitsev AV, Czanner G, Kroner S, Gonzalez-Burgos G, Povysheva NV, Iyengar S, Barrionuevo G, Lewis DA (2005) Cluster analysis-based physiological classification and morphological properties of inhibitory neurons in layers 2–3 of monkey dorsolateral prefrontal cortex. J. Neurophysiol. 94: 3009–3022.

Liley DTJ, Cadusch PJ, Dafilis MP (2002) A spatially continuous mean field theory of electrocortical activity. Network: Comput. Neural. Syst. 13: 67–113.

Mountcastle V (1997) The columnar organization of the neocortex. Brain. 120: 701–722.

Murakami S, Zhang T, Hirose A, Okada YC (2002) Physiological origins of evoked magnetic fields and extracellular field potentials produced by guinea-pig CA3 hippocampal slices. J. Physiol-London. 544: 237–251.

Netoff TI, Schiff SJ (2002) Decreased neuronal synchronization during experimental seizures. J. Neurosci. 15: 7297–7307.

Nowak LG, James AC, Bullier J (1997) Corticocortical connections between visual areas 17 and 18a of the rat studied in vitro: spatial and temporal organisation of functional synaptic responses. Exp. Brain. Res. 117: 219–241.

Nunez PL, Cutillo BA (eds) (1995) Neocortical dynamics and human EEG rhythms. Oxford University Press, New York.

Rutecki PA, Lebeda FJ, Johnston D (1987) 4-Aminopyridine produces epileptiform activity in hippocampus and enhances synaptic excitation and inhibition. J. Neurophysiol. 57: 1911–1924.

Singer W (1993) Synchronization of cortical activity and its putative role in information processing and learning. Annu. Rev. Physiol. 55: 349–374.

Steyn-Ross ML, Steyn-Ross DA, Sleigh JW, Whiting DR (2003) Theoretical predictions for spatial covariance of the electroencephalographic signal during the anesthetic-induced phase transition: Increased correlation length and emergence of spatial self-organization. Phys. Rev. E. 68: 021902.

Sutherling WW, Barth DS (1989) Neocortical propagation in temporal lobe spike foci on magnetoencephalography and electroencephalography. Ann. Neurol. 25: 373–381.

Traub RB, Contreras D, Cunningham MO, Murray H, LeBeau FEN, Bibbig A, Boyd S, Cross H, Baldweg T (2005) Single-column thalamocortical network model exhibiting gamma oscillations, sleep spindles, and epileptogenic bursts. J. Neurophysiol. 93: 2194–2232.

Weissinger F, Buchheim K, Siegmund H, Meierkord H (2005) Seizure spread through the life cycle: optical imaging in combined brain slices from immature, adult, and senile rats in vitro. Neurobiol. Dis. 19: 84–95.

Wilson HR, Cowan JD (1972) Excitatory and inhibitory interactions in localized populations of model neurons. Biophys. J. 12: 1–24.